Contents lists available at ScienceDirect

Energy Storage Materials

Copper silicate nanotubes anchored on reduced graphene oxide for long-life lithium-ion battery

Chunjuan Tang[a,b,1], Jiexin Zhu[a,1], Xiujuan Wei[a,1], Liang He[a], Kangning Zhao[a], Chang Xu[a], Liang Zhou[a,*], Bo Wang[b], Jinzhi Sheng[a], Liqiang Mai[a,*]

[a] State Key Laboratory of Advanced Technology for Materials Synthesis and Processing, Wuhan University of Technology, Wuhan 430070, Hubei, PR China
[b] Department of Mathematics and Physics, Luoyang Institute of Science and Technology, Luoyang 471023, PR China

ARTICLE INFO

ABSTRACT

Copper silicate (CSO) is a promising anode material for lithium-ion batteries (LIBs). It delivers high specific capacity; however, the capacity fades quickly because of its intrinsic poor electric conductivity and large volume variation during lithium ion insertion/extraction. Herein, a sandwich-like structure with CSO nanotubes grown on both sides of reduced graphene oxide (RGO) is designed to solve the capacity fading issue. The RGO not only serves as a soft and robust matrix to mitigate the large volume change during cycling but also acts as the electron highway. When applied as the anode material for LIBs, the as-obtained CSO/RGO sandwich-like structure exhibits high reversible capacity, good rate capability, and excellent cycling stability. A reversible capacity of 516 mA h g^{-1} can be achieved after 1000 cycles at 500 mA g^{-1}.

1. Introduction

As a predominant power source for portable electronics, LIBs have gained commercial success due to their high energy density and long cycle life [1–3]. The ever-growing energy demands of our society have inspired the exploration of new electrode materials with high safety, high reversible capacity, and good rate capability [4–8].

Metal silicates are a very attractive family of anode materials for LIBs because of their low cost, abundant reserves, environmental friendliness, easy synthesis, and high theoretical capacity [9–14]. Take $CuSiO_3$ as an example, each formula of $CuSiO_3$ may react with 6.4 Li^+ reversibly: $CuSiO_3 + 4 \ Li^+ + 4 \ e^- \rightarrow CuO + Si + 2 \ Li_2O$ (irreversible reaction), $CuO + 2 \ Li^+ + 2 \ e^- \leftrightarrow Cu + Li_2O$ (conversion reaction), and $Si + 4.4 \ Li^+ + 4.4 \ e^- \leftrightarrow Li_{4.4}Si$ (alloying/dealloying reaction) [13]. Combining the conversion reaction and alloying/dealloying reaction together, the theoretical capacity of $CuSiO_3$ reaches as high as 1229 mA h g^{-1}, which is three times higher than that of commercial graphite (372 mA h g^{-1}). This capacity is also comparable to typical metal oxide anode materials based on conversion reaction [15,16]. Although the theoretical capacity of $CuSiO_3$ is lower than that of Si (4200 mA h g^{-1}), the easy synthesis of $CuSiO_3$ might be a great advantage over Si.

However, metal silicates have been rarely investigated as anode materials. Yang *et al.* reported the lithium storage performance of nickel silicate [9]. It shows an initial discharge capacity of 1650 mA h g^{-1}. Although the high capacity is appealing, the fast capacity fading makes it difficult for practical applications. The fast capacity fading is ascribed to its intrinsic poor electric conductivity and large volume variation during lithium insertion/extraction. It is hypothesized that simultaneous improving the electronic conductivity and accommodating the volume variation may significantly enhance the cycling stability of metal silicates.

Combining active materials with RGO has been demonstrated to be an effective strategy to boost the electrochemical performance [17–20]. Various nanoparticles [21–25], nanoplates [26–30], and nanorods[31–33] have been grown onto RGO. To the best of our knowledge, there is no report on nanotubes anchored on RGO except for the carbon nanotube-RGO nanocomposites [34–36]. Herein, we report the synthesis of a novel sandwich-like structure with ultrafine CSO nanotubes grown on both sides of RGO. As the anode materials for LIBs, the as-obtained CSO/RGO manifests high reversible capacity, good rate capability, and excellent cycling stability. Specifically, the CSO/RGO composite delivers a capacity of 516 mA h g^{-1} after 1000 cycles at a current density of 500 mA g^{-1}.
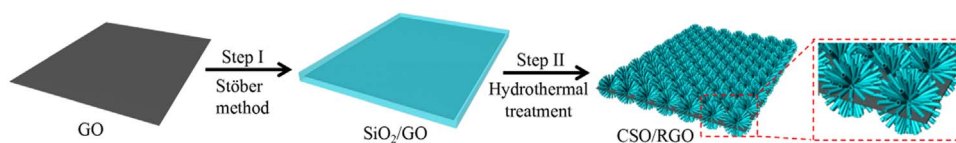
Fig. 1. Schematic illustration of the formation of CSO nanotubes anchored on RGO.

2. Experimental section

2.1. Materials synthesis

2.1.1. Synthesis of SiO₂/GO sandwich-like structure

GO is synthesized via a modified Hummers method [37]. For the synthesis of SiO₂/GO sandwich-like nanocomposite, hexadecyltri-methylammonium bromide (0.15 g) was added into the mixture of 120 mL ethanol and 30 mL deionized water, and stirred vigorously for 5 min. GO solution (10 mL, 3.95 mg mL^{-1}) was dispersed into the above solution and stirred for another 10 min. Then, 3 mL of concentrated $NH_3 \cdot H_2O$ (~28 wt%) was added into the solution. After that, 1 mL tetraethyl orthosilicate (TEOS) was added into the solution dropwise and stirred for 4 h. The resulting product was collected by centrifugation, washed with deionized water, and dried at 60 °C for 8 h. The SiO₂/GO composites obtained by adding 1 mL, 0.6 mL, and 0.3 mL TEOS are denoted as SiO₂/GO-1, SiO₂/GO-2, and SiO₂/GO-3, respectively.

2.1.2. Synthesis of CSO/RGO nanostructure

For the synthesis of CSO/RGO composite, 60 mg of SiO₂/GO-1 was dispersed into 35 mL deionized water with ultrasonication for 30 min. $Cu(NO_3)_2 \cdot 4H_2O$ (1.2 mmol), NH_4Cl (5 mmol) and $NH_3 \cdot H_2O$ (1 mL) were added into the solution in sequence under vigorously stirring. The solution was transferred into a 50 mL autoclave and maintained at 140 °C for 20 h. The black product was collected by centrifugation, washed with deionized water and ethanol, and dried at 60 °C for 6 h. The products synthesized using SiO₂/GO-1, SiO₂/GO-2, and SiO₂/GO-3 are denoted as CSO/RGO-1, CSO/RGO-2, and CSO/RGO-3, respectively. Pristine CSO is obtained by annealing CSO/RGO-1 in air at 450 °C for 6 h.

2.2. Materials characterization

D8 Advance X-ray diffractometer with a non-monochromated Cu Kα X-ray source was used to characterize the crystalline structure of the products. The morphology and microstructure were characterized with field emission scanning electron microscopy (SEM, JEOL-7100F) and transmission electron microscopy (TEM, JEM-2100F STEM/EDS). Brunauer-Emmet-Teller (BET) surface areas and pore size distributions were measured using Tristar II 3020 instrument. Raman spectra were obtained using a Renishaw IN VIA micro-Raman spectroscopy system. Thermogravimetric Analysis (TGA) was performed with Netzsch STA 449F3 at a heating rate of 10 °C min^{-1} in air.

2.3. Measurement of electrochemical performance

The electrochemical measurements were carried out using 2016 type coin cells assembled in the glove box filled with argon. Lithium chips were used as the counter electrode and reference electrode. The working electrode was prepared by mixing the active material, acetylene black, and carboxyl methyl cellulose (CMC) in a weight ratio of 70:25:5. The slurry was casted on the copper foil, dried at 70 °C for 4 h, then dried at 120 °C for 24 h in a vacuum oven. The mass loading of the active material was 1.0–1.5 mg cm^{-2}. 1 M LiPF₆ in a mixture of ethylene carbonate and dimethyl carbonate with the volume ratio of 1:1 was used as the electrolyte. Before the electrochemical test, the cell was placed at room temperature for at least 4 h. Galvanostatic discharge/charge measurements were performed in the potential window of 0.01–3 V *vs.* Li⁺/Li using a multichannel battery testing system (LAND CT2001A). Cyclic voltammetry (CV) and electrochemical impedance spectroscopy (EIS) were tested using electrochemical workstation (Autolab Potentiostat Galvanostat 302N and CHI760D). All of the measurements were carried out at room temperature.

3. Results and discussion

The sandwich-like CSO/RGO composite is prepared via a two-step process (Fig. 1). In step I, SiO₂ is coated on the surface of GO via a facile Stöber method. In step II, the as-obtained SiO₂/GO is converted into CSO/RGO composite by hydrothermal treatment, during which $NH_3 \cdot H_2O$, NH_4Cl, and $Cu(NO_3)_2 \cdot 4H_2O$ are introduced.

The morphologies and microstructures of the SiO₂/GO composites were studied by SEM. With the usage of 1.0 mL of TEOS, the SiO₂/GO-1 well inherits the nanosheet morphology of GO (Figure S1), indicating the uniform coating of SiO₂ on the surface of GO. When 1.2 mL of TEOS is used, both separate SiO₂ spheres and composite nanosheets can be observed in the product (Figure S2a and S2b), indicating that the amount of TEOS is excessive. When 0.6 mL of TEOS is used, the SiO₂/GO-2 composite shows thin nanosheet morphology with smooth surface (Figure S2c and S2d). When the amount of TEOS decreases to 0.3 mL, the SiO₂ is not enough to form a continuous coating; instead, it forms island-like domains on GO (Figure S2e and S2f). The above results indicate that SiO₂ can be homogeneously and conformally coated onto GO sheets by the hydrolysis and condensation of an appropriate amount of TEOS.

The crystal structure and phase of the product obtained via hydrothermal method is studied by X-ray diffraction (XRD). Fig. 2 shows the XRD pattern of the CSO/RGO-1. The peaks can be indexed to chrysocolla copper silicate (JCPDS No. 03-1152, $CuSiO_3 \cdot xH_2O$). All the diffraction peaks are broadened and the intensities are very low, indicating the low crystallinity of the sample. No diffraction peaks for RGO can be observed in the XRD pattern, which is ascribed to the highly dispersed nature and ultrathin feature of RGO [23].

The morphology and structure of the CSO/RGO-1 is characterized by SEM and TEM. During the hydrothermal reaction, the SiO₂ in SiO₂/GO composites is *in-situ* transformed into CSO, resulting in the formation of CSO/RGO composites. As shown in the SEM images
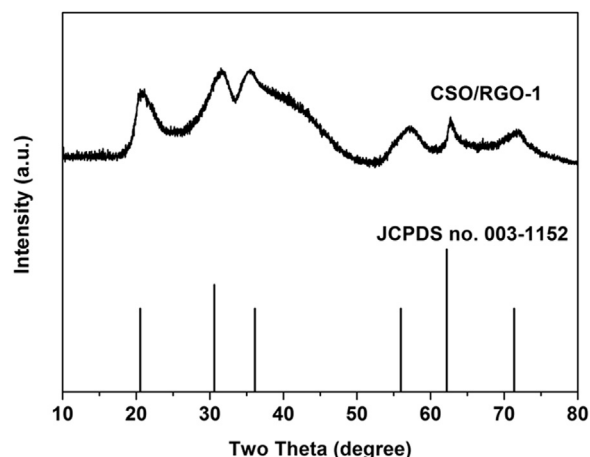

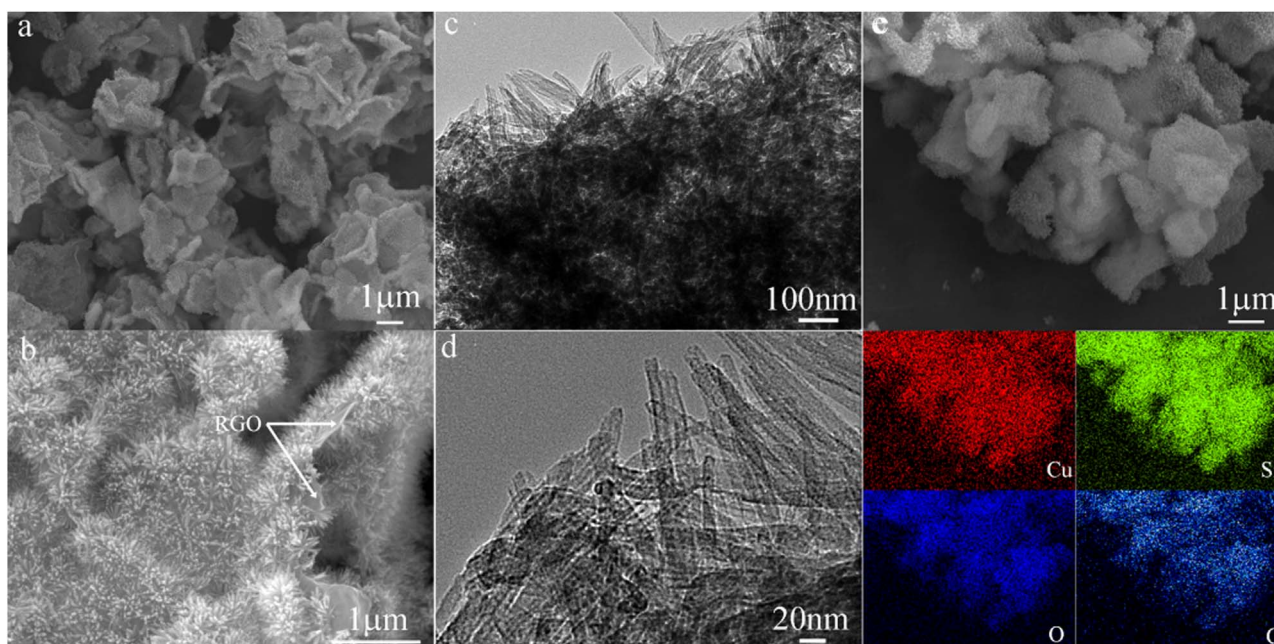**Fig. 2.** XRD pattern of CSO/RGO-1.

Fig. 3. SEM images (a, b), TEM images (c, d), elemental mapping (e) of CSO/RGO-1.

(Fig. 3a and 3b), CSO nanotubes cover the surface of RGO uniformly, forming a sandwich-like structure. The RGO sheets can only be observed at the edges of the composites under high magnifications (Fig. 3b). Fig. 3c and 3d show the TEM images of CSO/RGO-1. Agreeing with the SEM observations, the CSO nanotubes grow on the surface of RGO uniformly and densely. The diameters of the nanotubes are determined to be ~5 nm. High resolution TEM (HRTEM) image and selected area electron diffraction (SAED) pattern of CSO/RGO-1 are shown in Figure S3. Due to the low crystallinity, it is difficult to observe the lattice fringes of CSO nanotubes in the HRTEM image. A set of diffuse diffraction rings can be observed in the SAED pattern, further confirming the low crystallinity of CSO. Fig. 3e displays the energy dispersive X-ray spectroscopic (EDS) elemental mapping results, from where one can know the homogeneous distribution of Cu, Si, O, and C in the products. The EDS mapping results further confirm that the CSO nanotubes are uniformly grown on the surface of RGO. The Cu to Si ratio is determined to be 1 to 1 by EDS analysis (Figure S4), which is in consistency with the formula. For comparison, the morphologies and structures of CSO/RGO-2, CSO/RGO-3, and pristine CSO are also investigated and the results are shown in Figure S5 and S6. It is worth mentioning that the pristine CSO prepared by annealing CSO/RGO-1 in air at 450 °C shows a similar morphology to CSO/RGO-1 (Figure S6).

The highly porous feature of CSO/RGO-1 is characterized by N_2 sorption (Figure S7). The CSO/RGO-1 has a type IV adsorption-desorption isotherm (Figure S7a). The Brunauer-Emmett-Teller specific surface area of the product is as high as $387 \, m^2 \, g^{-1}$. The Barret-Joyner-Halenda pore size distribution (Figure S7b) displays a typical bimodal pore system. The small pore with a pore size of 2–3 nm is attributed to the inner diameter of the CSO nanotubes, while the large pore centered at ~30 nm is attributed to the packing voids. Such a porous structure would facilitate the penetration of electrolyte into the active material, and thus promote the electrochemical reactions and boost the electrochemical performance.

Raman spectrum of CSO/RGO-1 (Figure S8) presents two distinct carbonaceous peaks. The peaks centered at 1327 and $1593 \, cm^{-1}$ are ascribed to D-band and G-band, respectively. The D band is ascribed to the defect of C atoms and the G band is attributed to the stretching vibration of sp^2 C atoms. Figure S9 shows the thermogravimetric analysis results of CSO/RGO. According to the weight loss from 300 to 700 °C, the contents of RGO are estimated to be 2.2 wt%, 4.8 wt%, and 7.3 wt% for CSO/RGO-1, CSO/RGO-2, and CSO/RGO-3, respectively.

The electrochemical performances of CSO/RGO are studied by CV, galvanostatic discharge-charge test, and EIS. The first three CV curves of CSO/RGO-1 at a scan rate of $0.1 \, mV \, s^{-1}$ is shown in Fig. 4a. In the initial cathodic process, there is an obvious peak located at 1.3 V, which disappears in the subsequent cycles. It may be ascribed to the initial lithium ion insertion into the CSO/RGO-1 [38]. The difference between the 1st and 2nd cathodic processes indicates a highly irreversible reaction. In the initial anodic process, there are two peaks located at 2.0 and 2.8 V. The anodic peaks of the subsequent cycles overlap with those of the first cycle with slight change in the intensity.

Fig. 4b displays the discharge-charge profiles of CSO/RGO-1 at the current density of $200 \, mA \, g^{-1}$. A discharge plateau at 1.2–1.5 V can be seen clearly in the 1st cycle discharge curve; however, it disappears in the following cycles. This tendency is consist with that of CV profiles. And this phenomenon is very common for the alloy and conversion type anode materials [2,39–41]. The discharge and charge capacities of CSO/RGO-1 composite are 1557 and $818 \, mA \, h \, g^{-1}$, respectively. The irreversible capacity is as high as $739 \, mA \, h \, g^{-1}$, which is ascribed to the formation of SEI film and irreversible reaction ($CuSiO_3 \cdot xH_2O + 4Li^+ + 4e^- \rightarrow CuO + Si + 2Li_2O + xH_2O$). The discharge-charge curves of CSO and GO are presented in Figure S10. The curves of CSO are similar to those of CSO/RGO, indicating the identical electrochemical reaction.

Figure S11a shows the cycling performances of CSO/RGO-1, pristine CSO, and GO at the current density of $200 \, mA \, g^{-1}$. The capacity of CSO/RGO-1 is much higher than the other two. The higher capacity of sandwich-like CSO/RGO-1 is attributed to the synergistic effect between CSO and RGO. The RGO improves the electrical conductivity of the CSO effectively and the CSO nanotubes provide high capacity. EIS of CSO/RGO-1 and CSO are measured and shown in Figure S11b. The EIS for both CSO/RGO-1 and CSO are composed of a semicircle in the high frequency region and an inclined line in the low frequency region. The diameter of the semicircle represents the charge transfer resistance at the interface (R_{ct}). The slope of the line represents the diffusion constant of the lithium ions in the electrode materials. The semicircle diameter of CSO/RGO-1 is smaller than that of CSO, indicating the lower R_{ct}. The steeper slope of CSO/RGO-1 suggests the faster lithium ion diffusion rate in the electrode materials [27].
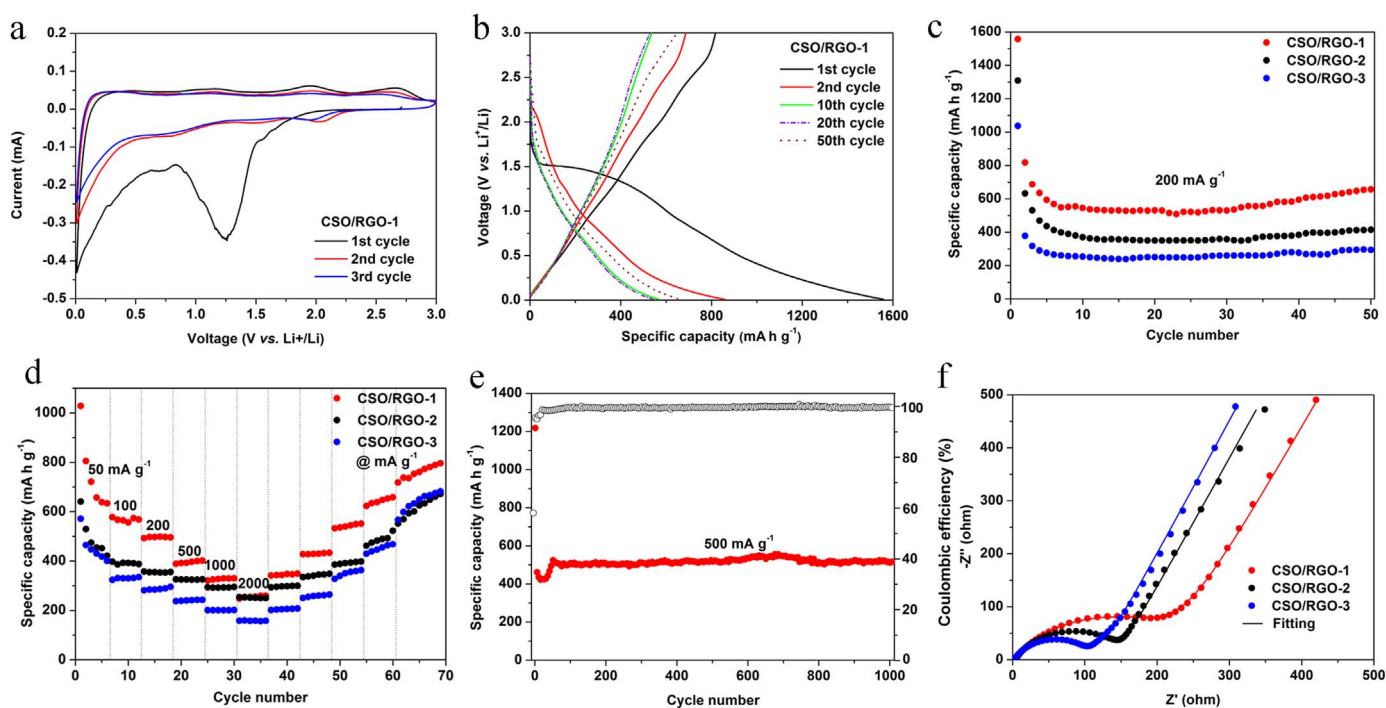
Fig. 4. (a) CV curves of CSO/RGO-1, (b) charge-discharge profiles of CSO/RGO-1 at the current density of 200 mA g^{-1}, (c) cycling performance of CSO/RGO at the current density of 200 mA g^{-1}, (d) rate performances of CSO/RGO (from the 2nd cycle), (e) cycling stability of CSO/RGO-1 at the current density of 500 mA g^{-1}, (f) EIS of CSO/RGO.

It is very important to know how the amount of RGO affects the electrochemical performance of the sandwich-like structures. Fig. 4c shows the cycling performance of CSO/RGO at the current density of 200 mA g^{-1}. All the electrode materials exhibit good stability during the cycling process, and CSO/RGO-1 displays the highest capacity, which is attributed to its highest CSO content. The capacities of the electrode materials firstly decrease and then increase by activation of the electrode material after cycling [42].

When tested at various current densities ranging from 50 to 2000 mA g^{-1}, CSO/RGO-1 displays higher capacity at each current than CSO/RGO-2 and CSO/RGO-3, demonstrating the superior rate performance (Fig. 4d). The reversible specific capacities for CSO/RGO-1 at current densities of 50, 100, 200, 500, 1000, and 2000 mA g^{-1} are 639, 574, 498, 400, 329, and 260 mA h g^{-1}, respectively. With the current density returned back to 50 mA g^{-1} after high current density testing, a reversible capacity of 773 mA h g^{-1} can be obtained, which is higher than the initial capacity at the same current density. Similar trend is observed in other two samples and has been reported for other metal silicate as well [27]. Compared to the previous report on CSO based anode materials [13], the CSO/RGO-1 delivers higher reversible capacities at low current densities (Table S1).

The long-life cycling performance of CSO/RGO-1 is evaluated at the current density of 500 mA g^{-1} (Fig. 4e). The first discharge and charge capacities are 1218 and 707 mA h g^{-1}, respectively. The capacity fades slightly during the first 20th cycles and then begins to rise due to the activation of electrode material. After the activation process, the capacity stabilizes at around 520 mA h g^{-1}. After 1000 cycles, a capacity of 516 mA h g^{-1} can be maintained, which demonstrates the outstanding cycling stability.

To attest the structural advantage of CSO/RGO-1 over pristine CSO, *ex-situ* SEM images after 1000 discharge-charge cycles are collected (Figure S12, S13). The sandwich-like structure of CSO/RGO-1 can be well retained, suggesting its excellent structural stability. In sharp contrast, the original sheet-like CSO (Figure S6) pulverizes into fine nanoparticles (Figure S13).

Fig. 4f shows the EIS of CSO/RGO to understand the excellent performances of the sandwich-like CSO/RGO-1. The R$_{ct}$ value for CSO/

RGO-3 is determined to be 55.7 Ω, which is smaller than that of CSO/RGO-2 (62.9 Ω) and CSO/RGO-1 (78.4 Ω). It can be concluded that both the specific capacity and R$_{ct}$ value decrease with the increasing of RGO content in the CSO/RGO composites. The results further prove that the capacity is afforded by the CSO nanotubes and the RGO acts as a conductive matrix. The excellent electrochemical performance of CSO/RGO-1 is attributed to the synergistic effect of high capacity CSO and highly conductive RGO with appropriate proportion.

4. Conclusions

A novel CSO nanotube-RGO sandwich-like nanocomposite has been synthesized via a facile hydrothermal method. The CSO nanotube provides high capacity; meanwhile, the RGO acts as soft and conductive matrix, enhancing the structural stability and conductivity of the nanocomposite. Due to the synergistic effect between high-capacity CSO nanotube and highly conductive RGO, the resultant CSO/RGO nanocomposite manifests high reversible capacity, good cycling stability, and excellent rate performance. A high capacity of 516 mA h g^{-1} can be achieved after 1000 cycles at 500 mA g^{-1}.

Appendix A. Supporting information

References

[1] C.J. Niu, J.S. Meng, C.H. Han, K.N. Zhao, M.Y. Yan, L.Q. Mai, VO_2 nanowires assembled into hollow microspheres for high-rate and long-life lithium batteries, Nano Lett. 14 (2014) 2873–2878.

[2] H.W. Zhang, L. Zhou, O. Noonan, D.J. Martin, A.K. Whittaker, C.Z. Yu, Tailoring the void size of iron oxide@carbon yolk–shell structure for optimized lithium storage, Adv. Funct. Mater. 24 (2014) 4337–4342.

[3] Y. Yao, M.T. McDowell, I. Ryu, H. Wu, N. Liu, L.B. Hu, W.D. Nix, Y. Cui, Interconnected silicon hollow nanospheres for lithium-ion battery anodes with long cycle life, Nano Lett. 11 (2011) 2949–2954.

[4] X. Zhou, L.J. Wan, Y.G. Guo, Binding SnO_2 nanocrystals in nitrogen-doped graphene sheets as anode materials for lithium-ion batteries, Adv. Mater. 25 (2013) 2152–2157.

[5] L.H. Hu, F.Y. Wu, C.T. Lin, A.N. Khlobystov, L.J. Li, Graphene-modified $LiFePO_4$ cathode for lithium ion battery beyond theoretical capacity, Nat. Comm. 4 (2013) 1687.

[6] Q.Y. An, F. Lv, Q.Q. Liu, C.H. Han, K.N. Zhao, J.Z. Sheng, Q.L. Wei, M.Y. Yan, L.Q. Mai, Amorphous vanadium oxide matrixes supporting hierarchical porous Fe_3O_4/graphene nanowires as a high-rate lithium storage anode, Nano Lett. 14 (2014) 6250–6256.

[7] J. Hwang, S.H. Woo, J.M. Shim, C. Jo, K.T. Lee, J. Lee, One-pot synthesis of tin-embedded carbon/silica nanocomposites for anode materials in lithium-ion batteries, ACS Nano 7 (2013) 1036–1044.

[8] K. Chang, W. Chen, L-cysteine-assisted synthesis of layered mos2/graphene composites with excellent electrochemical performances for lithium ion batteries, ACS Nano 5 (2011) 4720–4728.

[9] Y. Yang, Q.Q. Liang, J.H. Li, Y. Zhuang, Y.H. He, B. Bai, X. Wang, $Ni_3Si_2O_5(OH)_4$ multi-walled nanotubes with tunable magnetic properties and their application as anode materials for lithium batteries, Nano Res. 4 (2011) 882–890.

[10] F. Mueller, D. Bresser, N. Minderjahn, J. Kalhoff, S. Menne, S. Krueger, M. Winter, S. Passerini, Cobalt orthosilicate as a new electrode material for secondary lithium-ion batteries, Dalton Trans. 43 (2014) 15013–15021.

[11] J. Qu, Y. Yan, Y.X. Yin, Y.G. Guo, W.G. Song, Improving the Li-ion storage performance of layered zinc silicate through the interlayer carbon and reduced graphene oxide networks, ACS Appl. Mater. Interfaces. 5 (2013) 5777–5782.

[12] C.J. Tang, J.Z. Sheng, C. Xu, S.M.B. Khajehbashi, X.P. Wang, P. Hu, X.J. Wei, Q.L. Wei, L. Zhou, L.Q. Mai, Facile synthesis of reduced graphene oxide wrapped nickel silicate hierarchical hollow spheres for long-life lithium-ion battery, J. Mater. Chem. A 3 (2015) 19427–19432.

[13] X.J. Wei, C.J. Tang, X.P. Wang, L. Zhou, Q.L. Wei, M.Y. Yan, J.Z. Sheng, P. Hu, B.L. Wang, L.Q. Mai, Copper silicate hydrate hollow spheres constructed by nanotubes encapsulated in reduced graphene oxide as long-life lithium-ion battery anode, ACS Appl. Mater. Interfaces. 7 (2015) 26572–26578.

[14] W. Cheng, F. Rechberger, G. Ilari, H. Ma, W.I. Lind, M. Niederberger, Amorphous cobalt silicate nanobelts@carbon composites as a stable anode material for lithium ion batteries, Chem. Sci. 6 (2015) 6908–6915.

[15] C. Miao, M. Liu, Y.B. He, X.Y. Qin, L.K. Tang, B. Huang, R. Li, B.H. Li, F.Y. Kang, Monodispersed SnO_2 nanospheres embedded in framework of graphene and porous carbon as anode for lithium ion batteries, Energy Storage Mater. 3 (2016) 98–105.

[16] Z.J. Li, D.B. Kong, G.M. Zhou, S.D. Wu, W. Lv, C. Luo, J.J. Shao, B.H. Li, F.Y. Kang, Q.H. Yang, Twin-functional graphene oxide: compacting with Fe_2O_3 into a high volumetric capacity anode for lithium ion battery, Energy Storage Mater. 6 (2017) 98–103.

[17] H. Tang, J. Zhang, Y.J. Zhang, Q.Q. Xiong, Y.Y. Tong, Y. Li, X.L. Wang, C.D. Gu, J.P. Tu, Porous reduced graphene oxide sheet wrapped silicon composite fabricated by steam etching for lithium-ion battery application, J. Power Sources 286 (2015) 431–437.

[18] Q.D. Li, Q.L. Wei, Q.Q. Wang, W. Luo, Q.Y. An, Y.N. Xu, C.J. Niu, C.J. Tang, L.Q. Mai, Self-template synthesis of hollow shell-controlled Li_3VO_4 as a high-performance anode for lithium-ion batteries, J. Mater. Chem. A 3 (2015) 18839–18842.

[19] A.A. Mikhaylov, A.G. Medvedev, C.W. Mason, A. Nagasubramanian, S. Madhavi, S.K. Batabyal, Q. Zhang, J. Gun, P.V. Prikhodchenko, O. Lev, Graphene oxide supported sodium stannate lithium ion battery anodes by the peroxide route: low temperature and no waste processing, J. Mater. Chem. A 3 (2015) 20681–20689.

[20] K.N. Zhao, L. Zhang, R. Xia, Y.F. Dong, W.W. Xu, C.J. Niu, L. He, M.Y. Yan, L.B. Qu, L.Q. Mai, SnO_2 quantum dots@graphene oxide as a high-rate and long-life anode material for lithium-ion batteries, Small 12 (2016) 588–594.

[21] G.B. Zeng, N. Shi, M. Hess, X. Chen, W. Cheng, T.X. Fan, M. Niederberger, A general method of fabricating flexible spinel-type oxide/reduced graphene oxide nanocomposite aerogels as advanced anodes for lithium-ion batteries, ACS Nano 9 (2015) 4227–4235.

[22] W. Li, F. Wang, Y.P. Liu, J.X. Wang, J.P. Yang, L.J. Zhang, A.A. Elzatahry, D. Al-Dahyan, Y.Y. Xia, D.Y. Zhao, General strategy to synthesize uniform mesoporous TiO_2/graphene/ mesoporous TiO_2 sandwich-like nanosheets for highly reversible lithium storage, Nano Lett. 15 (2015) 2186–2193.

[23] S.L. Yang, C.Y. Cao, P.P. Huang, L. Peng, Y.B. Sun, F. Wei, W.G. Song, Sandwich-like porous TiO_2/reduced graphene oxide (rGO) for high-performance lithium-ion batteries, J. Mater. Chem. A 3 (2015) 8701–8705.

[24] Z.S. Wu, W.C. Ren, L. Wen, L.B. Gao, J.P. Zhao, Z.P. Chen, G.M. Zhou, F. Li, H.M. Cheng, Graphene anchored with Co_3O_4 nanoparticles as anode of lithium ion batteries with enhanced reversible capacity and cyclic performance, ACS Nano 4 (2010) 3187–3194.

[25] S.M. Paek, E.J. Yoo, I. Honma, Enhanced cyclic performance and lithium storage capacity of SnO_2/ graphene nanoporous electrodes with three-dimensionally delaminated flexible structure, Nano Lett. 9 (2009) 72–75.

[26] G.X. Gao, H.B. Wu, B.T. Dong, S.J. Ding, X.W. Lou, Growth of ultrathin $ZnCo_2O_4$ nanosheets on reduced graphene oxide with enhanced lithium storage properties, Adv. Sci. 2 (2015) 1400014.

[27] Q.Q. Wang, J. Qu, Y. Liu, C.X. Gui, S.M. Hao, Y.H. Yu, Z.Z. Yu, Growth of nickel silicate nanoplates on reduced graphene oxide as layered nanocomposites for highly reversible lithium storage, Nanoscale 7 (2015) 16805–16811.

[28] J. Zhu, Y.K. Sharma, Z. Zeng, X. Zhang, M. Srinivasan, S. Mhaisalkar, Q. Yan, Cobalt oxide nanowall arrays on reduced graphene oxide sheets with controlled phase, grain size, and porosity for li-ion battery electrodes, J. Phys. Chem. C 115 (2011) 8400–8406.

[29] J.W. Zhou, J. Qin, X. Zhang, C.S. Shi, E.Z. Liu, J.J. Li, N.Q. Zhao, C.N. He, 2D space-confined synthesis of few-layer MoS_2 anchored on carbon nanosheet for lithium-ion battery anode, ACS Nano 9 (2015) 3837–3848.

[30] B. Luo, Y. Fang, B. Wang, J.S. Zhou, H.H. Song, L.J. Zhi, Two dimensional graphene–SnS_2 hybrids with superior rate capability for lithium ion storage, Energy Environ. Sci. 5 (2012) 5226–5230.

[31] B. Zhao, R.Z. Liu, X.H. Cai, Z. Jiao, M.H. Wu, X.T. Ling, B. Lu, Y. Jiang, Nanorod-like Fe_2O_3/graphene composite as a high-performance anode material for lithium ion batteries, J. Appl. Electrochem. 44 (2014) 53–60.

[32] H.L. Wang, Y. Yang, Y.Y. Liang, L.F. Cui, H.M.S. Casalongue, Y.G. Li, G.S. Hong, Y. Cui, H.J. Dai, $LiMn_{1-x}Fe_xPO_4$ nanorods grown on graphene sheets for ultrahigh-rate-performance lithium ion batteries, Angew. Chem. 123 (2011) 7502–7506.

[33] M. Zhen, S. Guo, G. Gao, Z. Zhou, L. Liu, TiO_2−B nanorods on reduced graphene oxide as anode materials for Li ion batteries, Chem. Commun. 51 (2015) 507–510.

[34] Y.H. Xue, Y. Ding, J.B. Niu, Z.H. Xia, A. Roy, H. Chen, J. Qu, Z.L. Wang, L.M. Dai, Rationally designed graphene-nanotube 3D architectures with a seamless nodal junction for efficient energy conversion and storage, Sci. Adv. 1 (2015) 1400198.

[35] S.H. Lee, V. Sridhar, J.H. Jung, K. Karthikeyan, Y.S. Lee, R. Mukherjee, N. Koratkar, I.K. Oh, Graphene-nanotube-iron hierarchical nanostructure as lithium ion battery anode, ACS Nano 7 (2013) 4242–4251.

[36] J.R. He, Y.F. Chen, P.J. Li, F. Fu, Z.G. Wang, W.L. Zhang, Three-dimensional CNT/graphene–sulfur hybrid sponges with high sulfur loading as superior-capacity cathodes for lithium–sulfur batteries, J. Mater. Chem. A 3 (2015) 18605–18610.

[37] D.C. Marcano, D.V. Kosynkin, J.M. Berlin, A. Sinitskii, Z. Sun, A. Slesarev, L.B. Alemany, W. Lu, J.M. Tour, Improved synthesis of graphene oxide, ACS Nano 4 (2010) 4806–4814.

[38] R. Thomas, G.M. Rao, Phase and dimensionality of tin oxide at graphene nanosheet array and its electrochemical performance as anode for lithium ion battery, Electrochim. Acta 125 (2014) 380–385.

[39] H. Long, T. Shi, H. Hu, S. Jiang, S. Xi, Z. Tang, Growth of hierarchal mesoporous NiO nanosheets on carbon cloth as binder-free anodes for high-performance flexible lithium-ion batteries, Sci. Rep. 4 (2014) 7413.

[40] S. Chen, Y.L. Xin, Y.Y. Zhou, F. Zhang, Y.R. Ma, H.H. Zhou, L.M. Qi, Robust a-Fe_2O_3 nanorod arrays with optimized interstices as high-performance 3D anodes for high-rate lithium ion batteries, J. Mater. Chem. A 3 (2015) 13377–13383.

[41] J.W. Seo, J.T. Jang, S.W. Park, C. Kim, B. Park, J. Cheon, Two-dimensional SnS_2 nanoplates with extraordinary high discharge capacity for lithium ion batteries, Adv. Mater. 20 (2008) 4269–4273.

[42] W. Wen, J.M. Wu, Y.Z. Jiang, S.L. Yu, J.Q. Bai, M.H. Cao, J. Cui, Anatase TiO_2 ultrathin nanobelts derived from room-temperature-synthesized titanates for fast and safe lithium storage, Sci. Rep. 5 (2015) 11804.